UNIVERSITY OF BIRMINGHAM
University of Birmingham Research at Birmingham

HF Propagation Results From The Metal Oxide Space Cloud (MOSC) Experiment

Joshi, Dev; Groves, Keith; McNeil, William; Carrano, Charles ; Caton, Ronald; Parris, R Todd; Pedersen, Todd; Cannon, P.S.; Angling, Matthew; Jackson-Booth, Natasha

DOI:
10.1002/2016RS006164

License:
Other (please specify with Rights Statement)

Document Version
Peer reviewed version

Citation for published version (Harvard):
Joshi, D, Groves, K, McNeil, W, Carrano, C, Caton, R, Parris, RT, Pedersen, T, Cannon, PS, Angling, M & Jackson-Booth, N 2017, 'HF Propagation Results From The Metal Oxide Space Cloud (MOSC) Experiment', *Radio Science*, vol. 52, no. 6, pp. 710-722. https://doi.org/10.1002/2016RS006164

Link to publication on Research at Birmingham portal

Publisher Rights Statement:
Accepted for publication in Radio Science. Copyright (2017) American Geophysical Union. Further reproduction or electronic distribution is not permitted. See the publisher's version via http://onlinelibrary.wiley.com/doi/10.1002/2016RS006164/full
Eligibility for repository: Checked on 3/5/2017

General rights
Unless a licence is specified above, all rights (including copyright and moral rights) in this document are retained by the authors and/or the copyright holders. The express permission of the copyright holder must be obtained for any use of this material other than for purposes permitted by law.

•Users may freely distribute the URL that is used to identify this publication.
•Users may download and/or print one copy of the publication from the University of Birmingham research portal for the purpose of private study or non-commercial research.
•User may use extracts from the document in line with the concept of 'fair dealing' under the Copyright, Designs and Patents Act 1988 (?)
•Users may not further distribute the material nor use it for the purposes of commercial gain.

Where a licence is displayed above, please note the terms and conditions of the licence govern your use of this document.

When citing, please reference the published version.

Take down policy
While the University of Birmingham exercises care and attention in making items available there are rare occasions when an item has been uploaded in error or has been deemed to be commercially or otherwise sensitive.

If you believe that this is the case for this document, please contact UBIRA@lists.bham.ac.uk providing details and we will remove access to the work immediately and investigate.

Download date: 05. May. 2023

HF PROPAGATION RESULTS FROM THE METAL OXIDE SPACE CLOUD (MOSC) EXPERIMENT

Short title: **HF results from the MOSC experiment**

Dev Joshi[(1),(2)], Keith Groves[(1)], William McNeil[(1)], Charles Carrano[(1)], Ronald Caton [(3)] , R. Todd Parris[(3)] , Todd Pederson [(3)] , Paul Cannon[(4)] , Matthew Angling[(4)] , Natasha Jackson-Booth[(5)]

[(1)]Institute for Scientific Research, Boston College, MA USA
[(2)]Department of Physics, Boston College, MA USA
[(3)]Air Force Research Lab, Kirtland AFB, NM USA
[(4)]University of Birmingham, Birmingham, UK
[(5)]QinetiQ, Malvern, UK

Corresponding Author Information

Dev Raj Joshi

Institute for Scientific Research, Boston College, Newton, MA 02459

Room 218B, Kenny Cottle Hall

885 Centre Street, Newton, MA 02459

Phone: +1 617-552-1390

Email: dev.joshi@bc.edu

Key Points:

High Frequency Propagation effects due to an artificial plasma cloud successfully modeled

Effects of arbitrary plasma environments shown to be predicted with accuracy by ray-tracing

Ray tracing can be applied to selectively adjust ionospheric models effectively for HF applications

ABSTRACT

With support from the NASA sounding rocket program, the Air Force Research Laboratory (AFRL) launched two sounding rockets in the Kwajalein Atoll, Marshall Islands in May 2013 known as the Metal Oxide Space Cloud (MOSC) experiment. The rockets released samarium metal vapor at preselected altitudes in the lower F-region that ionized forming a plasma cloud. Data from ALTAIR incoherent scatter radar and high frequency (HF) radio links have been analyzed to understand the impacts of the artificial ionization on radio wave propagation. The HF radio wave ray-tracing toolbox PHaRLAP along with ionospheric models constrained by electron density profiles measured with the ALTAIR radar have been used to successfully model the effects of the cloud on HF propagation. Up to three new propagation paths were created by the artificial plasma injections. Observations and modeling confirm that the small amounts of ionized material injected in the lower-F region resulted in significant changes to the natural HF propagation environment.

1. INTRODUCTION:

Since the 1950s after the availability of rockets for research purposes, experiments have been conducted to inject various materials into the atmosphere for the purpose of creating perturbations to the ambient medium [*Bedinger et al.*, 1958; *Rosenberg*, 1963; *Corliss*, 1971; *Davis*, 1979; *Wand and Mendillo, 1984; Bernhardt et al*., 2012]. Such ionospheric modification experiments in the form of chemical releases have been used for various goals such as to measure neutral wind directions and shears, to detect plasma drift velocities and electric fields, to exploit the ionosphere as a plasma laboratory without walls, to modify the plasma density in the ionosphere to trigger larger scale phenomena, and many other uses [*Bernhardt*, 1987; *Hu et al*.,

2011; *Shuman et al*., 2015]. The Air Force Research Laboratory (AFRL) launched two sounding rockets in the Kwajalein Atoll, Marshall Islands, in May 2013 known as the Metal Oxide Space Cloud (MOSC) experiment. The sounding rockets, each carrying a payload of two 2.5 kg canisters of powdered samarium metal in a thermite mixture, released samarium metal vapor at dusk at 170 and 180 km altitude, respectively. A fraction of the samarium metal vapor ionized in the ambient environment creating an additional layer of plasma. The objectives of the experiments were to understand the dynamics, evolution and chemistry of Sm atoms in the earth's upper atmosphere and to understand the interactions of artificial ionization and the background plasma and measure the effects on high frequency (HF) radio wave propagation. A host of diagnostic instruments were used to probe and characterize the cloud including the ALTAIR incoherent scatter radar, multiple GPS and optical instruments, satellite radio beacons, and a dedicated network of high frequency (HF) radio links. [*Caton et al*., 2016]. In this paper, we report the results from the HF sounder observations and modeling those results with the ALTAIR radar data using the HF radio wave ray-tracing MATLAB toolbox PHaRLAP. The modeling results enable us to understand the changes caused by the samarium plasma cloud in the HF propagation environment and thus validate the extent to which we can model HF propagation for other specified plasma perturbations. We have developed a new technique to model an anomalous background ionosphere by assimilating oblique ionosonde data specifically to match observed HF signal delays. The approach may have numerous applications for ionospheric specification for HF propagation.

In Figure 1, the site locations corresponding to the HF links and the ALTAIR incoherent scatter radar are shown. In this work, we focus on the signals received at Wotho from transmitters at

Rongelap and Likiep. The Rongelap-Wotho link geometry is predominantly N-S and the release region is far from the great-circle path, whereas the Likiep-Wotho path is nearly magnetic E-W and the release point lies close to the mid-point of the link. Geographic coordinates for the sites may be found in Table 1.

The 1st sounding rocket launch occurred on 1 May 2013 at 07:38 UT and the samarium metal vapor release occurred at 07:40:40 UT. The 2nd sounding rocket launch occurred on 9 May 2013 at 07:23 UT and the release occurred at 07:25:40 UT. In both releases, approximately 10% of the samarium metal in the canisters ionized.

2. OBSERVATIONS:

The Advanced Research Projects Agency Long-Range Tracking and Instrumentation Radar (ALTAIR) at Kwajalein Atoll was used to monitor the ionospheric state and track the evolution of the metal oxide space cloud. Range-time-intensity displays of each release event are shown in Figure 2. The data gap during the first release shown in Figure 2a was an intentional data management action to avoid a data file size limitation. Recording was turned off for a period of about two minutes and turned back on approximately 30 seconds prior to the samarium release. Improved pre-launch file management on the night of 9 May precluded the need to limit data sampling during the second rocket flight as shown in Figure 2b.

The ionograms (Figures 3 and 4) from the oblique sounder data for the releases on 1 and 9 May 2013 show the evolution of the ionosphere before and after the release of the samarium metal vapor in the ambient environment. Both Likiep and Rongelap used broadband folded dipole transmit antennas approximately 12-meters long connected to 100-Watt power amplifiers to transmit swept frequency waveforms from 2-30 MHz every five minutes at the rate of 100

KHz/sec. The timing for both transmitters and receivers was synchronized by GPS-disciplined clocks. The ionograms shown in the figures were recorded at Wotho using a simple 1-meter diameter loop antenna. Plots show data from only 2-14 MHz since no signatures were observed at higher frequencies. The titles include the start time of the frequency sweep (2 MHz); end time at 14 MHz is 120 seconds later. In pre-release sweeps on May 1, E-layer traces are also seen in the ionograms in addition to the ground wave and F-region traces whereas the E-layer trace isn't seen on May 9 suggesting the E-region is not present during the second release. The E-layer echoes present on 1 May are due to sporadic E [*Davies*, 1990], as the traces extend to 10 MHz or so, well beyond the peak plasma frequency expected in the E-region at this local time (approximately 18:20 LT). The F-region traces are further seen to be split into two characteristic components: ordinary and extra-ordinary waves. The effects of the artificial plasma cloud are clearly seen in the post-release sweeps along both Rongelap-Wotho and Likiep-Wotho paths. Two additional traces, denoted as the "MOSC" layer and the secondary F-region echo are evident, suggesting significant change in the propagation environment of the HF radio waves due to the metal oxide plasma cloud. SmO+ layer density (approximately 10 MHz at early times) is similar in both cases and observed initially on all links. The density of the artificial cloud is observed to fall rapidly over time scales of a few minutes and the signatures disappear completely within about fifteen minutes. The difference between the secondary F-region echo and F-region trace is smaller along the Likiep-Wotho path compared to the Rongelap-Wotho path, the reason of which is explained in the Section 4.2. A more detailed description of the cloud's evolution can be found in Pedersen et al., [2016]; here we focus on modeling the HF propagation observed during the first few minutes after the release. The SmO+ plasma also triggered significant modification of HF propagation in the F-region.

In the first post-release frequency sweep initiated less than 40 seconds after the release on 1 May, the Likiep-Wotho path has a MOSC signature only in the high end of the frequency sweep above f = 8 MHz (Fig. 3d), yet the Rongelap link shows a robust signature beginning at less than 4 MHz (Fig. 3c). The subsequent sweep five minutes later shows a solid MOSC trace at lower frequencies only on both paths (Fig 3e-f). Moreover, MOSC signature is present across most of the frequency band on both links in the second release during all phases of the observations (Fig. 4c-f). Potential reasons for the lack of signals on the Likiep-Wotho path in the lower portion of the HF frequency band during the first release will be discussed later in this paper.

3. MODELING:

Since *Haselgrove* (1955) set down the differential equations governing ray paths in an anisotropic medium for numerical integration techniques [*Haselgrove*, 1955], the equations have been used extensively [*Jones and Stephenson,* 1975; *Coleman,* 1993; *Zawdie et al.,* 2016] to study the propagation of HF energy through the ionosphere. In our work to model the HF sounder observations, we have used PHaRLAP, a HF radio wave ray tracing MATLAB toolbox developed by Dr. Manuel Cervera, that contains a variety of ray tracing engines of various sophistication from 2-D ray tracing to full 3-D magnetoionic ray tracing [*Cervera and Harris*, 2014].

Modeling the sounder observations involved insertion of a three-dimensional plasma cloud representing the MOSC into a background ionosphere and then using full 3-d magneto-ionic ray-tracing to understand the various propagation modes induced by introduction of Sm+ ions in the

ambient plasma. Prior to the first release on 1 May the ionosphere was rising rapidly ($v_z \geq 50$ m/sec), potentially responding to a minor magnetic perturbation (DST ~ -50), and spread F formed within minutes after the release as observed in the sounder data and ALTAIR radar scan. For the second release, the ionosphere was quiescent as seen in the sounder observations and the radar scan. Hence, we present the modeling efforts for the background ionosphere and samarium cloud for the second release in Section 3.1 before those for the first release (Section 3.2).

At early times immediately after the release, the cloud appeared to be symmetric optically and the ALTAIR radar scan also showed a symmetric density profile [*Caton, et al*., 2016]. Before- and after-release density profiles along with the symmetric 3D representation for the samarium plasma cloud derived from ALTAIR are shown in Figure 5 where a pre-release electron density profile (5a) and a post-release profile (5b) clearly show the contribution of the samarium plasma. A model cloud based on these observations was inserted into the background ionosphere for ray-tracing. A graphical representation of the digitized cloud is shown in Figure 5c while a false-color image of the cloud itself is shown in 5d. The image was acquired with the AFRL bare CCD camera through a 630-nm filter approximately 4 minutes after release. The cloud still appears spherical at this time which corresponds to the end of the first post-release HF frequency scans presented in Figure 4.

An ionospheric model was used for the background because we did not have adequate knowledge of the ionosphere across the whole region of interest. The approach was to constrain the background model with calibrated ALTAIR radar observations at a specific location and then use the model to represent the ionosphere across a region that extended approximately 200 km north and ± 200 km E-W from the point of the radar observations. We used the Parametrized

Ionospheric Model (PIM) [*Daniell et al*., 1995] and the International Reference Ionosphere (IRI-2012) [*Bilitza, et al.,* 2014] as the background model ionospheres for ray-tracing. The reason for using two models rather than just one will be made clear shortly.

The IRI is an empirical model ionosphere developed as a joint project of the Committee on Space Research (COSPAR) and the International Union of Radio Science (URSI). For a given location, time, and date, IRI provides the median monthly values of electron density, the electron temperature, and ion composition in the altitude range 50 km to 2000 km. The major data sources for the IRI model are the worldwide network of ionosondes, the powerful incoherent scatter radars, (Jicamarca, Arecibo, Millstone Hill, Malvern, St. Santin), the International Satellites for Ionospheric Studies (ISIS) and Alouette topside sounders, and in situ instruments on several satellites and rockets.

The PIM is a global ionospheric and plasmaspheric model based on combined output from the Global Theoretical Ionospheric Model (GTIM) model for low and middle latitudes. PIM produces electron density profiles between 90 and 25000 km altitude, in addition to other profile parameters such as corresponding critical frequencies and heights for the ionospheric E and F2 regions, and Total Electron Content (TEC).

3.1 Ionospheric Model for Samarium Release on 9 May

For the second release in which the background ionosphere exhibited typical quiescent characteristics, good agreement between the PIM model and the ALTAIR radar observations were obtained by making a small change in the F10.7 flux input to the model, as shown in Figure

184 6. The objective was to obtain a good fit primarily to the bottomside to insure accurate HF
185 propagation modeling.
186
187 **3.2 Ionospheric Model for Samarium Release on 1 May**
188 For the first release which had a disturbed and rapidly rising ionosphere, no standard model
189 could be fitted to match the background ionosphere. We tried to minimize the difference between
190 the model ionospheric profile and ALTAIR radar profile at the MOSC release location by an
191 optimization technique known as the Nelder-Mead Downhill Simplex method [*Nelder and Mead*,
192 1965; *Press et al.,* 2007]. We used the native "fminsearch" function in MATLAB to optimize the
193 difference between the ALTAIR radar ionospheric profile and the model profile (Fig 7a). Since
194 PIM didn't have enough accessible degrees of freedom, this optimization technique gave good
195 results only with the IRI model. An altitude-dependent scale vector was obtained by dividing the
196 optimized IRI profile by the initial IRI profile and this was subsequently used to scale the entire
197 IRI 3D grid. However, when the optimized results were used on the Rongelap-Wotho path
198 (approx. 150 km NW of ALTAIR scan), the modeled delay did not match observations with
199 sufficient accuracy, presumably because the disturbed ionosphere gradients were not well
200 represented by the scaled climatological model output. After experimenting with a number of
201 approaches we succeeded in modeling the background ionosphere along the raypath by applying
202 frequency-specific multipliers to the altitude-dependent scale vector; results are shown in Figure
203 7b. The variations in the multipliers were not large but they facilitated a good fit between the
204 modeled and observed profiles. The multipliers were determined by adjusting the ionosphere
205 using ray tracing to minimize the difference between the observed and modeled signal delays.
206 The primary objective is not to develop a good model of the ionosphere, but rather to optimize

our ability to model the HF propagation environment. The priority is for the primary F-region modes to match the observations with high fidelity so when the samarium cloud is introduced one can have high confidence in the propagation model results.

4. HF Propagation Modeling Results and Discussion

Ray-tracing was performed for both the releases after inserting the 3-D plasma cloud into the background ionosphere. It confirmed and explained the changes in propagation modes of the HF radio waves due to the artificial plasma cloud.

4.1 Rongelap-Wotho Path

As shown in Figure 8a, the Rongelap-Wotho path is nearly N-S and the release point is well off the great circle path connecting the two atolls. Up to three additional paths due to the presence of the samarium plasma cloud for the received HF energy have been identified. Rays reflected directly from the transmitter off the cloud account for the low delay MOSC trace. Meanwhile the secondary F-region traces may be formed in two ways. One path consists of reflection first by the F-layer to the MOSC cloud and subsequent reflection to the receiver site (high elevation). The other path is defined by waves that propagate directly to the samarium cloud, reflect to the F-region and are then reflected to the receiver (low elevation). The elevation angles so defined refer to the angle between the transmitted HF signal and the ground at the transmitter. Figure 8b shows a graphical representation of the various propagation modes identified to model the time delays shown in Figure 8c. The match between the observations and the model results suggest that both the high and low elevation angle paths contributed to the observed F-region secondary

228 layers. We note that the low elevation propagation mode corresponds to smaller delay compared
229 to that of the high elevation propagation mode in the F-region secondary trace (Fig. 8c). This is
230 as expected as the low elevation mode has a shorter path. From the geometry all the observed
231 signatures confirm that the cloud scattered and/or refracted HF energy well off the great circle
232 path. Rays were traced for a number of selected frequencies. Ray-tracing gave excellent results
233 which agree with the sounder observations (Fig. 8c and 8d). For the first release (Fig. 8d), the
234 additional MOSC and F-region secondary layers are also modeled to be close to the observed
235 layers validating the modeling approach and the technique developed to build a disturbed
236 background ionosphere.
237 For both the releases, the sounder observations show greater frequency extent for both the
238 MOSC samarium layer and the F-region secondary layer than the model results. Reasons for the
239 discrepancy include inadequate spatial resolution of the MOSC plasma cloud in the model and a
240 low estimate of the peak plasma density in the cloud obtained from the radar observations. The
241 high density center of the cloud is contained in a layer just a few hundred meters on a side, which
242 represents a very small target for ray tracing calculations, particularly for accurately homing rays
243 from a transmitter to a receiver. In fact, it is challenging to resolve the structure adequately in
244 both space and time with the ALTAIR radar. The observations presented in Figure 5b are the true
245 cloud density convolved spatially with the radar beam width and pulse resolution and the time
246 period over which the measurements were integrated. The measurements provide a good estimate
247 of the average parameters of the cloud over a 60-second window, but they do not represent a
248 precise characterization of the plasma cloud at the sub-kilometer resolution needed to describe
249 the structure in full detail. This does not present a critical problem, however, because the primary
250 objectives to identify and characterize the new propagation modes introduced by the cloud can

be achieved without an extremely high fidelity representation of the electron density in the cloud. The radar-derived spatial and plasma parameters are sufficient for this purpose.

4.2 Likiep-Wotho Path

Similar analysis was performed along the Likiep-Wotho path, shown in Figure 9a. This path was selected because the samarium release point lies nearly at the mid-point of the great circle path between the transmitter (Likiep) and the receiver (Wotho). The same modes to/from the cloud and the F-region were observed in this geometry, but the differences in delay between the normal F-layer path and the delayed paths (F-region to cloud; cloud to F-region) were significantly smaller than for the Rongelap-Wotho geometry as expected due to the co-planar geometry (see Fig 9b). Rays traced for various frequencies reproduced the additional MOSC and F-region secondary layers close to the observations for both releases (Fig. 9). As mentioned previously, one significant feature of the observations that remains to be explained is the absence of lower frequency signals (below ~ 8 MHz) refracted directly from the samarium cloud to the receiver on the Likiep-Wotho path within the first few minutes post-release on 1 May 2013.

The lack of lower frequency signals on the nearly-great circle path is noteworthy because relatively strong lower frequency signals are observed on the distinctly non-great circle Rongelap-Wotho link at the same time. Moreover lower frequency signals are present on both links throughout the observing period during the 2nd release on 9 May. One possible explanation is enhanced absorption during the early scan period on the Likiep-Wotho path. This absorption is frequency-dependent and would normally be associated with an enhanced E- or D-region not expected to be present at the time of the observations (18:47 SLT). A comparison of the relative intensities of the F-region traces at frequencies below 8 MHz clearly shows that there is little to no difference between the 1st and 2nd post-release scans on 1 May or the scans from the 2nd

274 release on 9 May. Absorption does not appear to be a viable mechanism for the observed absence
275 of power.

276 The primary geophysical difference between the 01 May and the 09 May releases was the
277 presence of sporadic E (Es) on the night of the first release. A reasonably strong Es layer is
278 visible on the Rongelap-Wotho link (Figures 3a, c, e) extending to about 10 MHz frequency. A
279 faint Es trace may be observed during the same time on the Likiep-Wotho path. On neither path
280 does the layer appear to be blanketing in terms of masking the F-region returns or the return from
281 the samarium cloud on the Rongelap path. But that does not preclude the possibility that the path
282 to the samarium cloud from Likiep, which is significantly different than the direct paths to both
283 the F and E regions, may have been partially or wholly obscured by local sporadic E at the lower
284 frequencies consistent with the lack of power observed below 6 MHz on the night of 01 May.
285 The severity of the effect may have been exacerbated by the reduced received power at low
286 frequencies on the Likiep-Wotho path relative to the Rongelap-Wotho path. HF transmissions at
287 Likiep were weaker overall than those from Rongelap and considerably weaker at frequencies
288 below 8 MHz. In fact, between 2-6 MHz the observed average signal strengths at Wotho were
289 more than 20 dB below the corresponding signals from Rongelap, as shown in Figure 10. The
290 curve in the Figure shows the ratio of power from Likiep/Rongelap as a function of frequency
291 and was derived from averaging ten scans during different quiet periods characterized by an
292 absence of Spread F and low E-region density. A straight line fit to the data is also plotted to
293 demonstrate the trend of the frequency dependence. Differences in path length between the two
294 sites account for some of the observed SNR differences, approximately 6(2.5) dB for E (F)
295 region paths, respectively. A more significant contribution to the disparity may result from the
296 transmit antenna installations at the two sites. The antenna at Rongelap was mounted on a tower

297 some 18-meters above ground, while the Likiep antenna was suspended from trees at a height of
298 just 4-meters. Although we do not have sufficient details to calculate the exact differences in
299 gain at the two sites, it is well known that the impedance of a dipole antenna changes
300 dramatically as the installation height decreases below ¼ wavelength (see e.g., ARRL Antenna
301 Handbook); the resulting impedance mismatch greatly reduces the radiation efficiency of the
302 antenna. The 18-meter height of the antenna at Rongelap corresponds to ¼ wavelength at about
303 4.2 MHz; the 4-meter high antenna at Likiep would transmit much less efficiently at this
304 frequency, though the relative response would be expected to improve rapidly as the frequency
305 increases, as has been observed. Similarly, one would expect the masking efficiency of Es to
306 decrease as the transmitted frequency increases. Thus, we believe a combination of factors
307 including path-length, antenna efficiency and Es masking effectiveness were responsible for the
308 absence of lower frequency signals scattered by the samarium cloud from Likiep on the evening
309 of 01 May. Of course, differences in the path lengths and antenna efficiencies were common to
310 all the observations, while sporadic E was present only during the first release. However, the
311 reduced signal strengths imposed by the common propagation factors from Likiep mean that
312 relatively modest Es masking is needed to explain the observations.
313
314 A high density plasma sphere placed in a low density plasma background behaves as a divergent
315 lens for radio waves; the signals will always be refracted away from the center. The top panel of
316 Figure 11 shows such a simulated sphere while the bottom panel displays the relative signal
317 strength for a 8-MHz plane wave traveling from left to right in the Figure. The propagation
318 results, derived from a wave-optics calculation [*Hocke and Igarashi*, 2003], show clearly how
319 the power diverges as the wave propagates through the sphere. In this scenario it is plausible that

the power from waves below 8-MHz was refracted off-axis passing through the samarium cloud and was not received along the great circle path at Wotho; signals at higher frequencies would suffer less refraction and could thus reach Wotho. Meanwhile the same plasma cloud could refract (or scatter) energy through acute angles such that signals from Rongelap were observed far off the great circle path, consistent with the actual observations. A detailed analysis of the cloud and geometry for the MOSC releases was performed. The results show that the region where refractive effects would be most effective in creating a signal void ("shadow") lies beyond Wotho. Indeed, the ray tracing results shown in Figure 9d specifically predict a signature at the lower frequencies where none is observed. Although it is treated as a sphere in our model, the actual shape and density distribution of the cloud determine the detailed HF propagation effects. Some elongation along the magnetic field is expected, even at early times, and the true shape undoubtedly differs from our simple model. Interestingly the divergent effects of the cloud would be expected to persist much longer than the effects visible on the oblique ionograms shown in Figures 3 and 4. The divergence effect requires only small refraction angles along the direction of propagation, while large refraction angles are required to generate traces directly from the artificial plasma cloud. Thus even signals at frequencies well above the maximum plasma frequency in the cloud will experience some level of divergence as they pass through.

5. CONCLUSIONS

The results presented here account for the features of the modified HF propagation environment observed at early times during the MOSC samarium release experiments. We have shown that ray tracing techniques may be used to model the disturbances caused by artificial ionospheric modification. The samarium plasma clouds created at least three additional HF propagation paths in the ionosphere. One path is directly from the transmitter to the cloud to the receiver, while two

344 others involve propagation between the F-region and the cloud; in one case interacting with the
345 cloud first, reflecting off the F-region to the receiver, and in the other reflecting from the F-
346 region first and then reaching the receiver antenna by refraction from the cloud. These effects
347 were observed both on a great circle path and a markedly non-great circle path where the
348 refraction angle exceeds 90°. Additionally, a drop-out in the lower portion of the HF band was
349 observed on the great circle path between Likiep and Wotho minutes after the first release. An
350 analysis of several potential causes reveals that the most probable explanation is masking due to
351 sporadic E which is exacerbated by the greater distance from Likiep to Wotho and the lower
352 transmitted signal power relative to Rongelap.
353 For modeling the background plasma, when constrained by ALTAIR radar electron density
354 profiles, the Parameterized Ionospheric Model (PIM) provided an excellent representation of the
355 low latitude ionosphere during quiet conditions. Not surprisingly, neither PIM nor IRI were able
356 to accurately specify local gradients during a modest magnetic disturbance. However, IRI's
357 flexibility and convenient access to parameters within the model supported the use of a
358 minimization technique for constructing a valid regional ionosphere. Ray tracing confirms the
359 sounder observations to a high degree of fidelity. Changes in the natural propagation
360 environment can thus be successfully modeled, and the effects from arbitrary artificial plasma
361 environments can be predicted with accuracy. Finally, though not observed directly in these
362 measurements, modeling predicts that the samarium cloud will behave like a divergent lens
363 resulting in "HF voids" or shadow zones where the HF signal is excluded downstream from the
364 sphere. For the geometry in the present experiment the shadow zones are predicted to lie beyond
365 the range of the most distant receiver site, but such effects could readily be characterized in
366 future experiments.

Acknowledgement.

Authors from the Boston College Institute for Scientific Research gratefully acknowledge support through the Naval Postgraduate School from the National Consortium for Measurement and Signature Intelligence (MASINT) Research Program, Award No.: N00244-12-1-0049. We would also like to acknowledge the valuable contributions of the reviewers to this manuscript, specifically in regard to the role of sporadic E in interpreting the propagation results (Reviewer #2). Requests for access to data collected during the MOSC experiment will be processed on a case-by-case basis pursuant to official Air Force Research Laboratory policy for public release of information.

REFERENCES

The ARRL Antenna Handbook (1974) Ed. Gerald Hall, 13th ed., Newington, CT: American Radio Relay League, 1974, p.50.

Bedinger, J. F., E. R. Manring, and S. N. Ghosh (1958), Study of sodium vapor ejected into the upper atmosphere, *J. Geophys. Res., 63*(1)*,* 19-29, doi: 10.1029/JZ063i001p0019.

386 Bernhardt, P. A. (1987), A critical comparison of ionospheric depletion chemicals, *J. Geophys.*
387 *Res., 92*(A5)*,* 4617–4628, doi: 10.1029/JA092iA05p04617.
388 Bernhardt, P. A., et al. (2012), Ground and space-based measurement of rocket engine burns in
389 the ionosphere, *IEEE Trans. Plasma Sci., 40,* 1267-1286, doi: 10.1109/TPS.2012.2185814.
390 Bilitza, D., D. Altadill, Y. Zhang, C. Mertens, V. Truhlik, P. Richards, L.-A. McKinnell, and B.
391 Reinisch (2014), The International Reference Ionosphere 2012 – a model of international
392 collaboration, *J. Space Weather Space Clim*. *4*, A07, doi: 10.1051/swsc/2014004.
393 Caton, R.G., T.R. Pedersen , K.M. Groves , J. Hines , P.S. Cannon , N. Jackson-Booth , J.M.
394 Holmes , R.T. Parris , Y-J Su , E.V. Mishin , P.A. Roddy , A.A. Viggiano , N.S. Shuman, S.G.
395 Ard , P.A. Bernhardt , C.L. Siefring , J. Retterer, E. Kudeki, and P.M. Reyes, Artificial
396 Ionospheric Modification – The Metal Oxide Space Cloud Experiment (2016), Radio Sci., in
397 press, DOI: 1002/2016RS005988.
398 Cervera, M. A., and T. J. Harris (2014), Modeling ionospheric disturbance features in quasi-
399 vertically incident ionograms using 3-D magnetoionic ray tracing and atmospheric gravity
400 waves, *J. Geophys. Res. Space Physics*, *119*, 431–440, doi: 10.1002/2013JA019247.
401 Coleman, C. J. (1993), A general purpose ionospheric ray tracing procedure, *Tech. Rep.,* SRL-
402 0131-TR, Defence Science Technology Organization, Adelaide, Australia.
403 Corliss, W.R. (1971), NASA sounding rockets, 1958–1968: A historical summary. *Technical*
404 *Report NASA SP- 4401,* National Aeronautics and Space Administration, Washington, D.C.
405 Davies, K. (1990), *Ionospheric Radio*, The Institute of Engineering and Technology
406 Davis, T.N. (1979), Chemical releases in the ionosphere, *Rep. Prog. Phys.*, *42*, 1565, doi:
407 10.1088/0034-4885/42/9/003.

Daniell, R. E., Jr., L. D. Brown, D. N. Anderson, M. W. Fox, P. H. Doherty, D. T. Decker, J. J. Sojka, and R. W. Schunk (1995), Parameterized ionospheric model: A global ionospheric parameterization based on first principles models, *Radio Sci*., *30*(5), 1499–1510, doi:10.1029/95RS01826.

Haselgrove, J. (1955), Ray Theory and a new method for raytracing, in *Physics of the Ionosphere,* pp. 355-364, Physical Society, London.

Hocke, K., and K. Igarashi (2003), Wave-optical simulation of the oblique HF radio field, Radio Sci., 38(3), 1039, doi:10.1029/2002RS002691.

Hu, Y., Z. Zhao, and Y. Zhang (2011), Ionospheric disturbances produced by chemical releases and the resultant effects on short-wave ionospheric propagation, J. Geophys. Res., 116, A07307, doi: 10.1029/2011JA016438.

Jones, R. M., and J. J. Stephenson (1975), A versatile three-dimensional ray tracing computer program for radio waves in the ionosphere, *NASA STI/Recon Tech. Rep., 76,* 25,476, U.S. Department of Commerce, Off. of Telecommun., Washington, D. C.

Nelder, J. and R. Mead (1965), "A simplex method for function minimization", *Computer Journal*, *7*, 749-756, doi: 10.1093/comjnl/7.4.308.

Pedersen, T. R., R. Caton , D. Miller , J. M. Holmes, K. M. Groves, Empirical modeling of plasma clouds produced by the Metal Oxide Space Clouds (MOSC) experiment (2016), in press, DOI: 10.1002/2016RS006079.

Press, W. H., S. A. Teukolsky, W. T. Vetterling, and B. P. Flannery (2007), Numerical Recipes 3rd Edition: The art of scientific computing, *Cambridge University Press,* New York.

429 Rosenberg, N. W. (1963), Chemical releases in the upper atmosphere (Project Firefly), A
430 summary report. *Geophys. Res., 68*(10), 3057–3063, doi: 10.1029/JZ068i010p03057.

431 Shuman, N. S., D. E. Hunton, and A. A. Viggiano (2015), "Ambient and Modified Atmospheric
432 Ion Chemistry: From Top to bottom," *Chem. Rev.*, *115* (10), pp 4542–4570, doi:
433 10.1021/cr5003479.

434 Wand, R. H., and M. Mendillo (1984), Incoherent scatter observations of an artificially modified
435 ionosphere, *J. Geophys. Res*., *89*(A1), 203–215, doi: 10.1029/JA089iA01p00203.

436 Zawdie, K. A., D. P. Drob, J. D. Huba, and C. Coker (2016), Effect of time-dependent 3-D
437 electron density gradients on high angle of incidence HF radio wave propagation, *Radio Sci., 51*,
438 1131–1141, doi: 10.1002/2015RS005843.

439

440

441

442

443

444 **Table 1**

Site	Latitude (°N)	Longitude (°E)
Rongelap	11.152	166.838
Likiep	9.826	169.307
Wotho	10.174	166.005

ALTAIR	9.395	167.479

445

446

447 **Figure 1:** Site Locations in Marshall Islands. Tx = Transmitter, Rx = Receiver. The MOSC
448 release point is mid-way between Likiep and Wotho.

449 **Figure 2: a) First release:** The ALTAIR radar range-time-intensity (RTI) plot (top panel) shows
450 a rapidly rising F-layer of the ionosphere (disturbed condition).
451 **b) Second release:** The RTI plot (bottom panel) shows a quiescent ionosphere typical of the
452 equatorial region just prior to the onset of the pre-reversal enhancement period.

453

454 **Figure 3: First Release:** Sounder Observations of the ionosphere before and after the release of
455 the samarium metal vapor along Rongelap-Wotho path (left column, panels a, c, e) and along
456 Likiep-Wotho path (right column, panels b, d, f).

457

458 **Figure 4: Second Release:** Sounder Observations of the ionosphere before and after the release
459 of the samarium metal vapor along Rongelap-Wotho path (left column, panels a, c, e) and along
460 Likiep-Wotho path (right column, panels b, d, f).

461

462 **Figure 5: a)** The ALTAIR radar profile before the release of the samarium metal vapor
463 b) The radar profile approximately 30 seconds post-release c) The two dimensional view of the
464 model cloud through its center is shown. The central pixel corresponds to f_{pe} = 7.44 MHz; and d)
465 a false-color image of the illuminated cloud acquired with the AFRL bare CCD all-sky imager

approximately four minutes after release on 9 May 2013. The cross-hair indicates the look-angle of the ALTAIR radar.

Figure 6: PIM and ALTAIR radar electron density (N_e) profiles displayed as equivalent plasma frequency ($f_p \approx \sqrt{N_e}$, in MKS units). The PIM bottomside fits well with the observed ATLAIR profile. The disparity below about 225 km corresponds to a very low density/frequency ($< 10^3$ cm^{-3} / 1 MHz) that will not have an appreciable effect on radio waves propagating above about 2 MHz.

Figure 7: a) The Nelder-Mead Downhill Simplex method applied to optimize IRI in the vicinity of ALTAIR radar data b) A second frequency dependent optimization procedure was applied to assimilate the sounder data along the R-W path.

Figure 8: a) Rongelap-Wotho geometry; b) Various Propagation modes for 6 MHz in Second Release; Excellent agreement between model and observations c) second release and d) first release

Figure 9: a) Likiep -Wotho geometry; b) Various Propagation modes for 6 MHz in Second Release; Close agreement between model and observations c) second release and d) first release

Figure 10. HF power received at Wotho from Likiep relative to Rongelap as a function of signal frequency (Likiep/Rongelap). The straight line shows a linear fit of the data. The received power from Rongelap was considerably higher at low frequencies.

Figure 11: Top panel: background environment and plasma distribution for a spherical artificial cloud. Bottom panel: Wave-optics calculation for 8 MHz radio wave propagation through the artificial cloud.

Figure 1.

Transmitter/Receiver Geometry

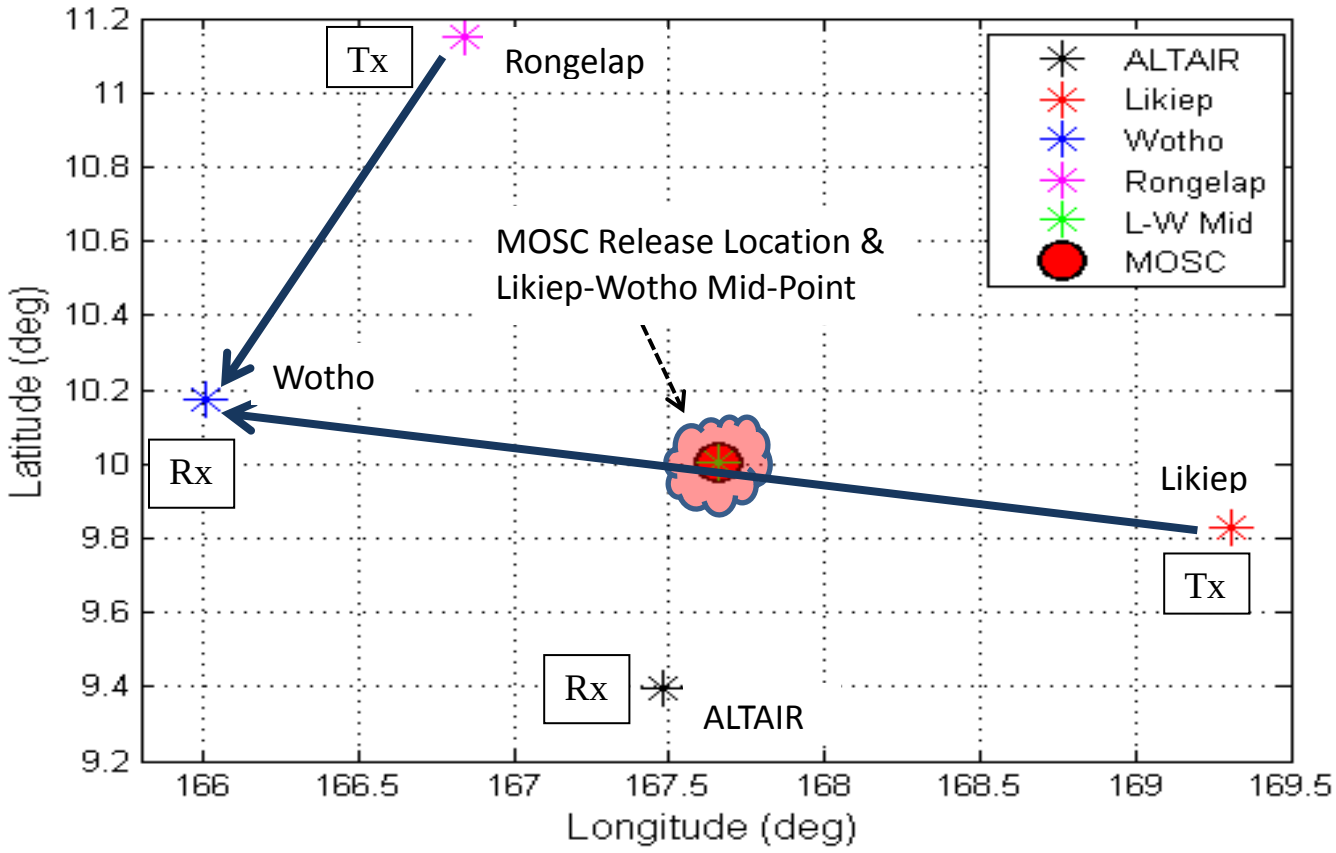

Figure 2.

a)

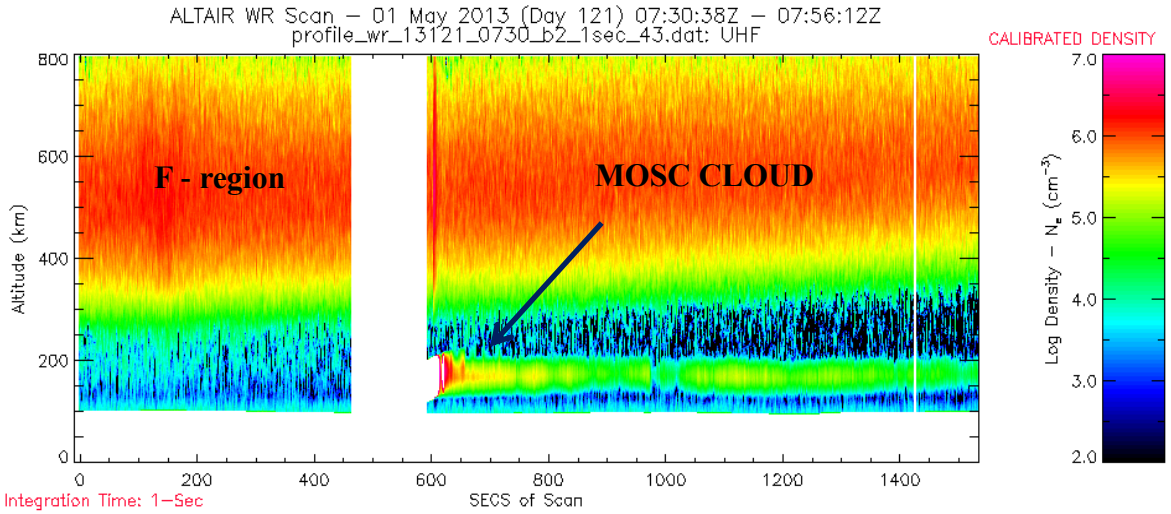
ALTAIR WR Scan – 01 May 2013 (Day 121) 07:30:38Z – 07:56:12Z
profile_wr_13121_0730_bZ_1sec_43.dat: UHF
CALIBRATED DENSITY
F - region
MOSC CLOUD
Altitude (km)
Log Density – N_e (cm^{-3})
SECS of Scan
Integration Time: 1–Sec

b)

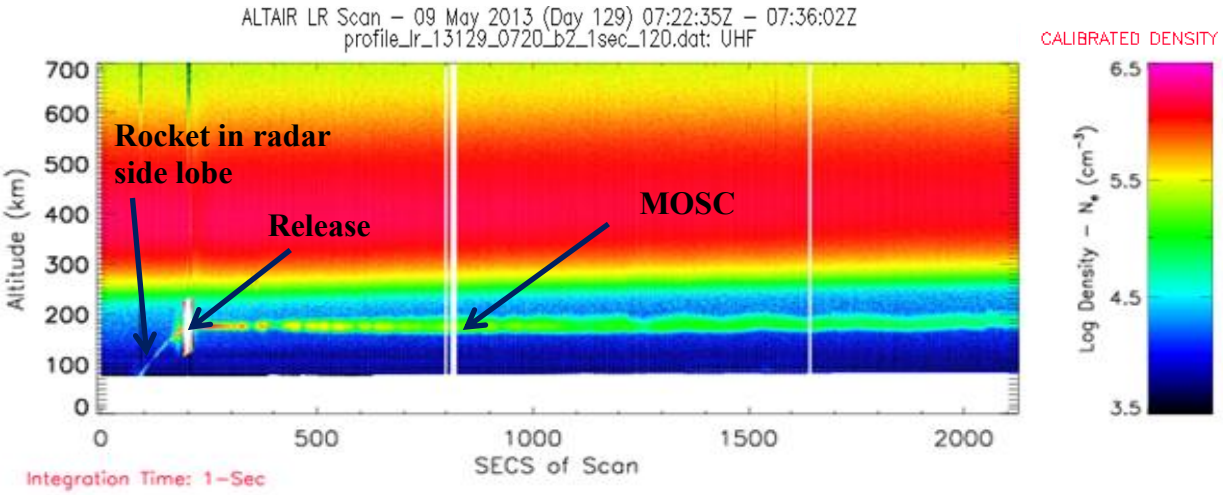
ALTAIR LR Scan – 09 May 2013 (Day 129) 07:22:35Z – 07:36:02Z
profile_lr_13129_0720_bZ_1sec_120.dat: UHF
CALIBRATED DENSITY
Rocket in radar side lobe
Release
MOSC
Altitude (km)
Log Density – N_e (cm^{-3})
SECS of Scan
Integration Time: 1–Sec

Figure 3.

Rongelap Wotho Path **Likiep Wotho Path**

Pre-Release Sweeps

a)

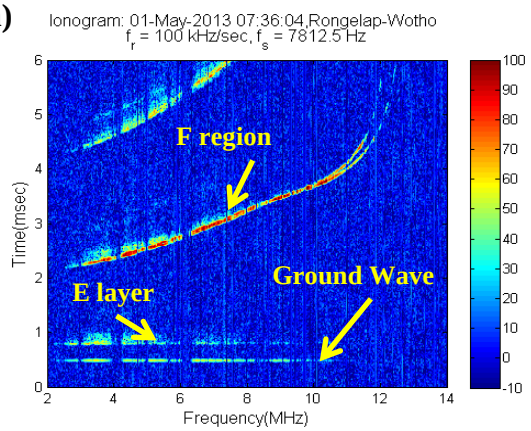

b)

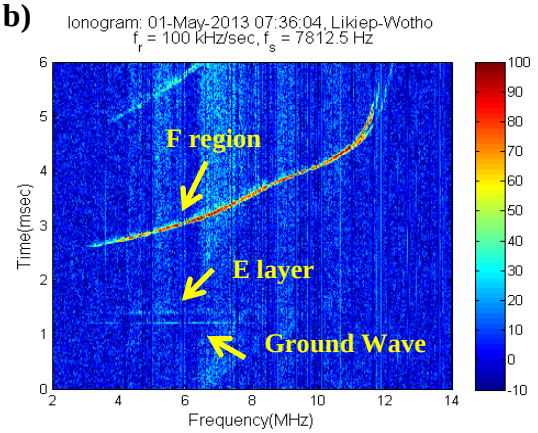

First Post-Release Sweeps

c)

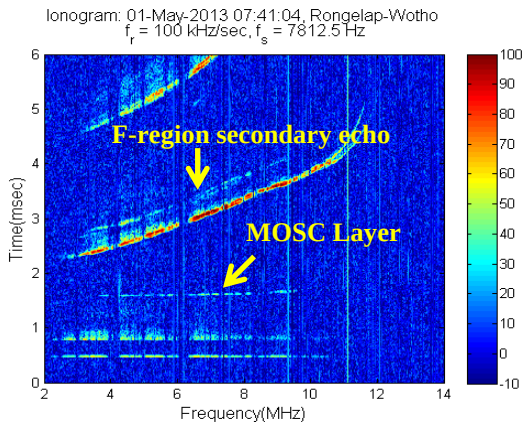

d)

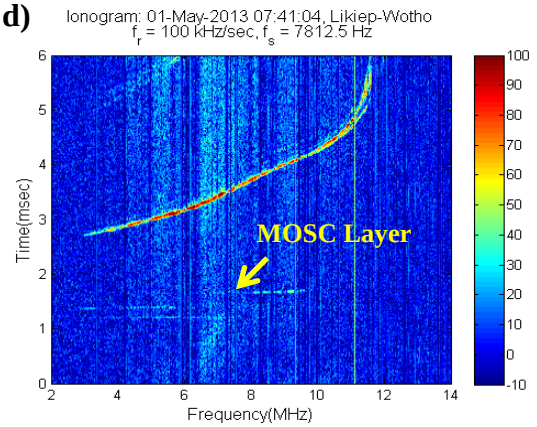

Second Post-Release Sweeps

e)

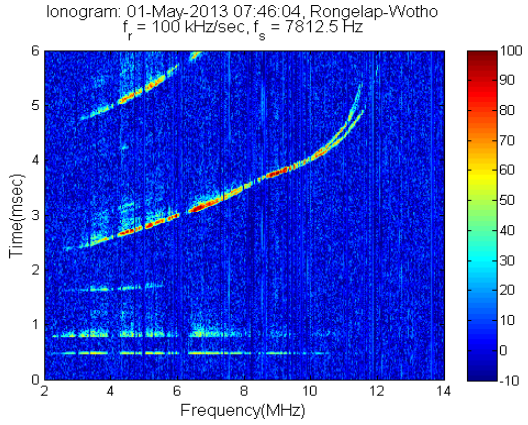

f)

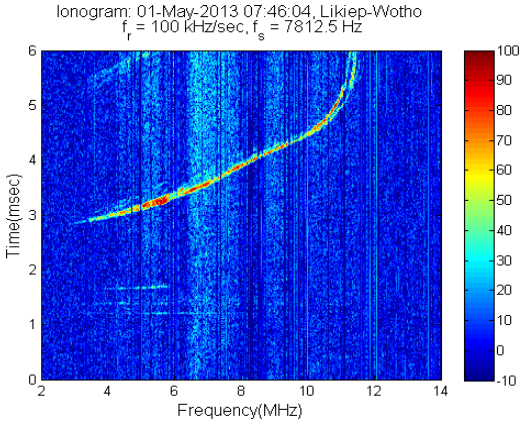

Figure 4.

Rongelap Wotho Path **Likiep Wotho Path**

Pre–Release Sweeps

a)

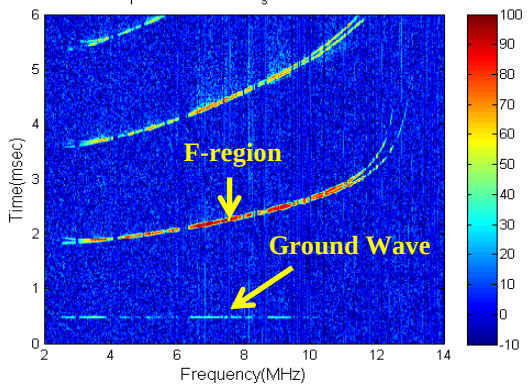

b)

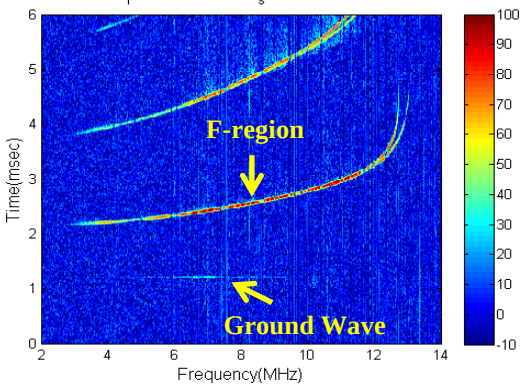

First Post-Release Sweeps

c)

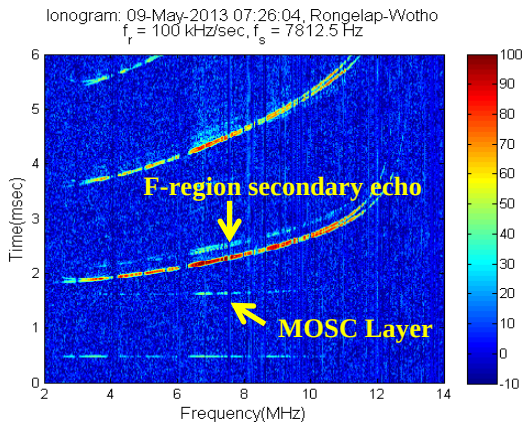

d)

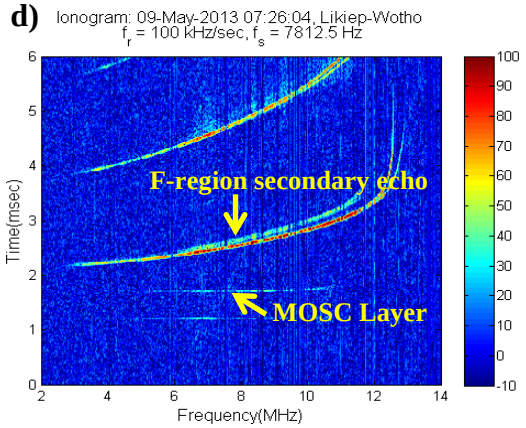

Second Post-Release Sweeps

e)

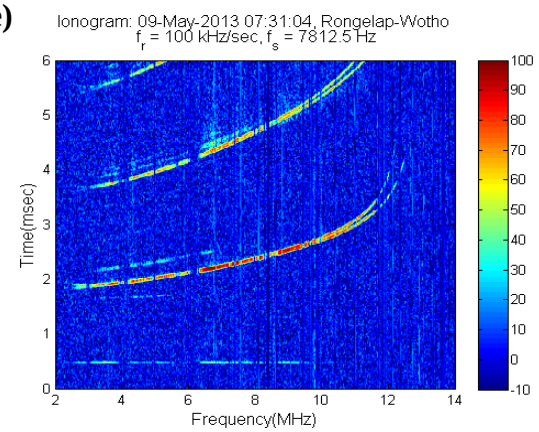

f)

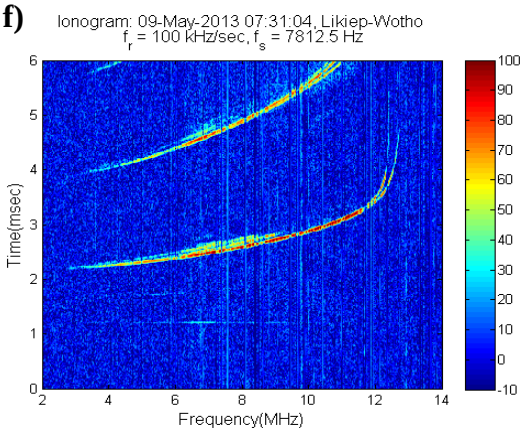

Figure 5.

a)

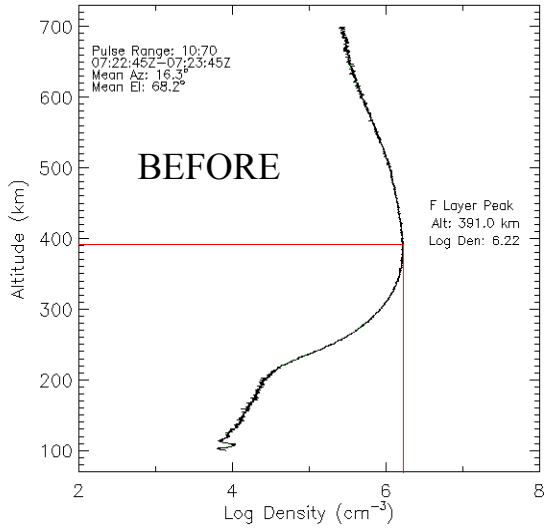
Pulse Range: 10:70
07:22:45Z–07:23:45Z
Mean Az: 16.3°
Mean El: 68.2°
BEFORE
F Layer Peak
Alt: 391.0 km
Log Den: 6.22
Altitude (km)
Log Density (cm⁻³)

b)

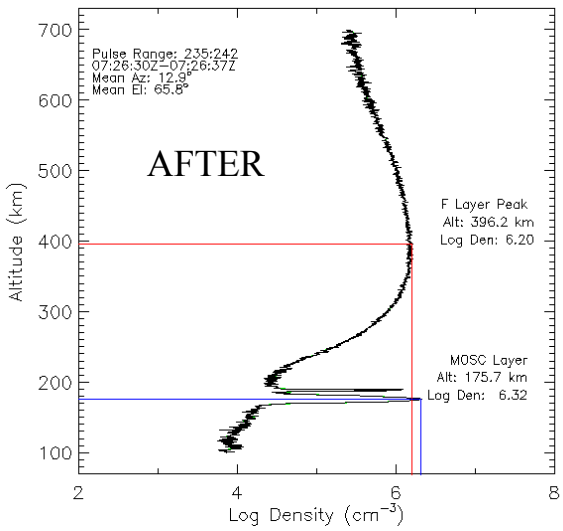
Pulse Range: 235:242
07:26:30Z–07:26:37Z
Mean Az: 12.9°
Mean El: 65.8°
AFTER
F Layer Peak
Alt: 396.2 km
Log Den: 6.20
MOSC Layer
Alt: 175.7 km
Log Den: 6.32
Altitude (km)
Log Density (cm⁻³)

c)

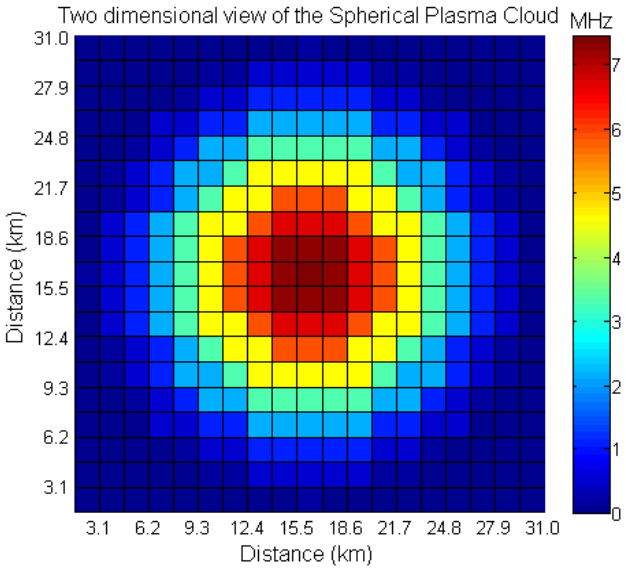
Two dimensional view of the Spherical Plasma Cloud
MHz
Distance (km)
Distance (km)

d)

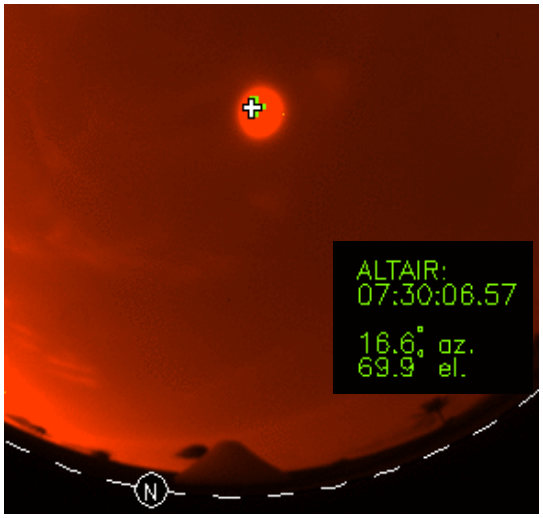
ALTAIR:
07:30:06.57
16.6° az.
69.9° el.
N

Figure 6.

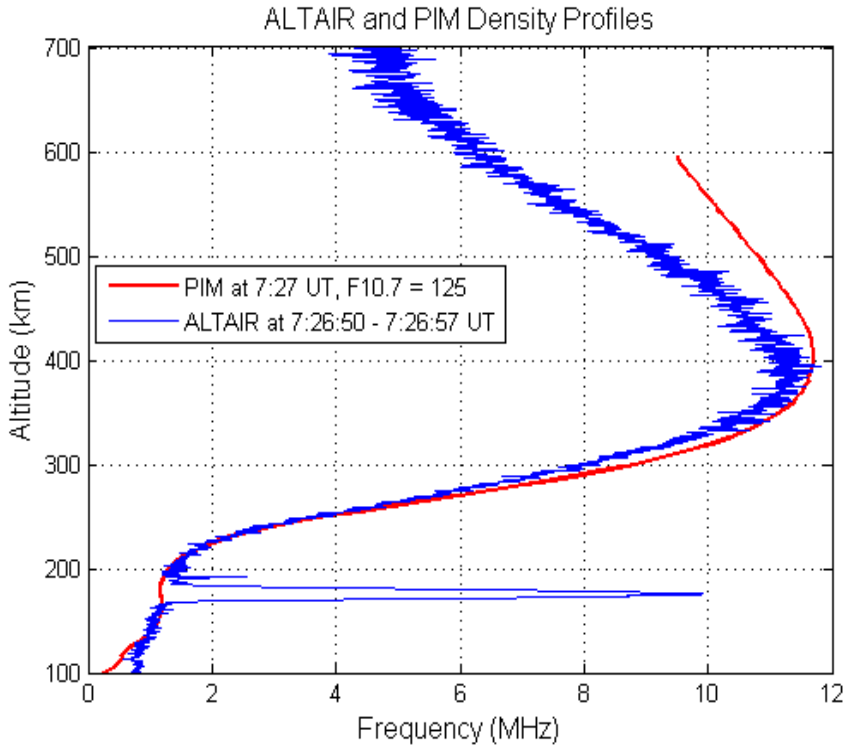
ALTAIR and PIM Density Profiles
PIM at 7:27 UT, F10.7 = 125
ALTAIR at 7:26:50 - 7:26:57 UT
Altitude (km)
Frequency (MHz)
700
600
500
400
300
200
100
0
2
4
6
8
10
12

Figure 7.

a)

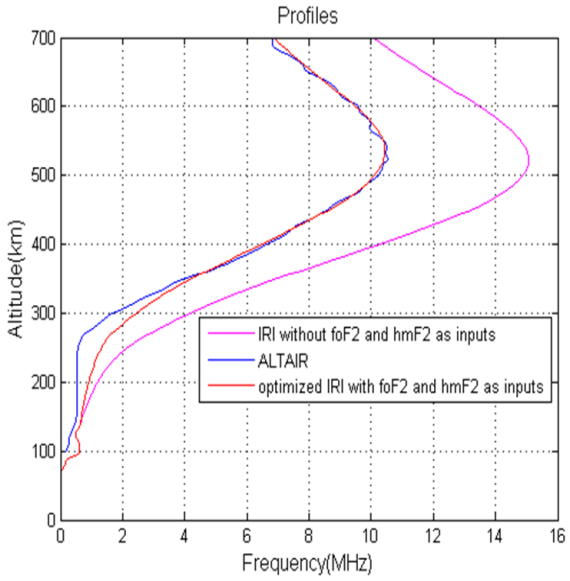
Profiles
Altitude(km)
Frequency(MHz)
IRI without foF2 and hmF2 as inputs
ALTAIR
optimized IRI with foF2 and hmF2 as inputs

b)

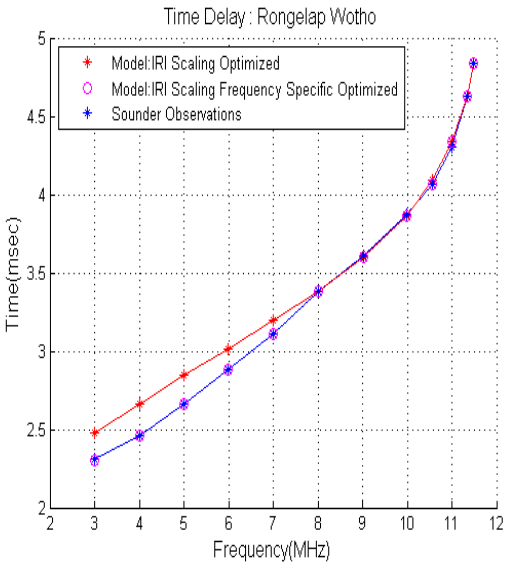
Time Delay : Rongelap Wotho
Time(msec)
Frequency(MHz)
Model:IRI Scaling Optimized
Model:IRI Scaling Frequency Specific Optimized
Sounder Observations

Figure 8.

a)

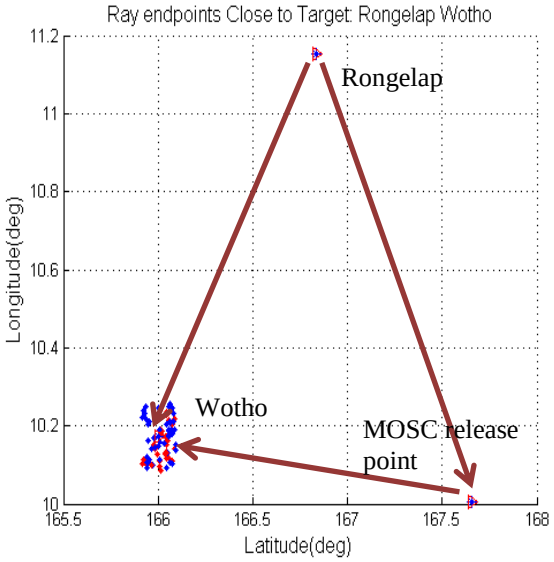
Ray endpoints Close to Target: Rongelap Wotho
Rongelap
Wotho
MOSC release point
Longitude(deg)
Latitude(deg)

b)

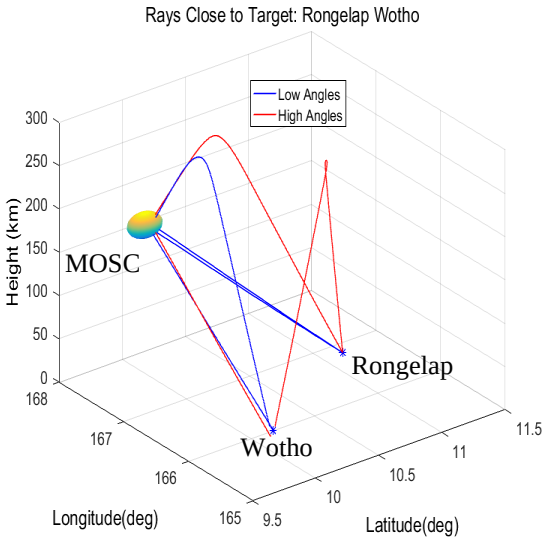
Rays Close to Target: Rongelap Wotho
Low Angles
High Angles
MOSC
Rongelap
Wotho
Height (km)
Longitude(deg)
Latitude(deg)

c)

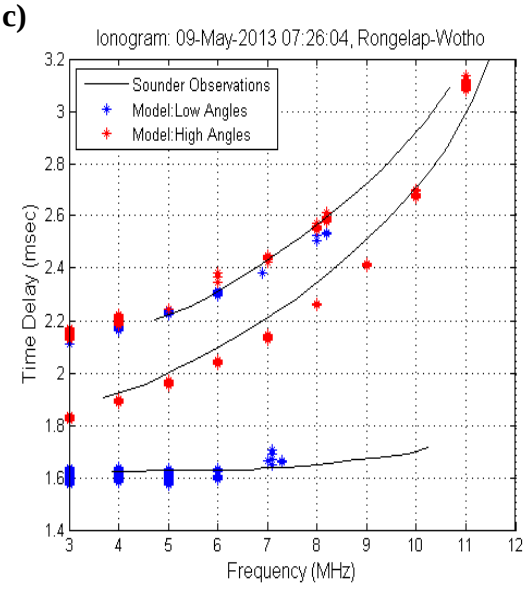
Ionogram: 09-May-2013 07:26:04, Rongelap-Wotho
Sounder Observations
Model:Low Angles
Model:High Angles
Time Delay (msec)
Frequency (MHz)

d)

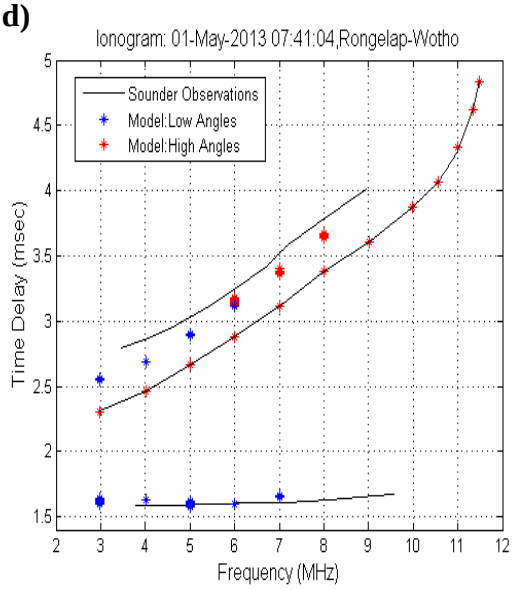
Ionogram: 01-May-2013 07:41:04,Rongelap-Wotho
Sounder Observations
Model:Low Angles
Model:High Angles
Time Delay (msec)
Frequency (MHz)

Figure 9.

a)

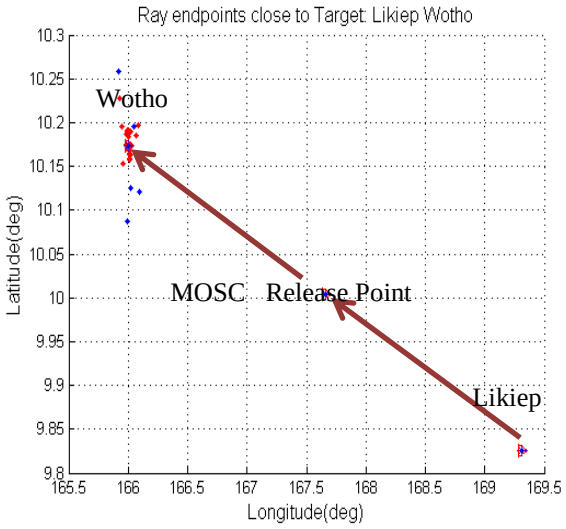
Ray endpoints close to Target: Likiep Wotho
Wotho
MOSC
Release Point
Likiep
Latitude(deg)
Longitude(deg)

b)

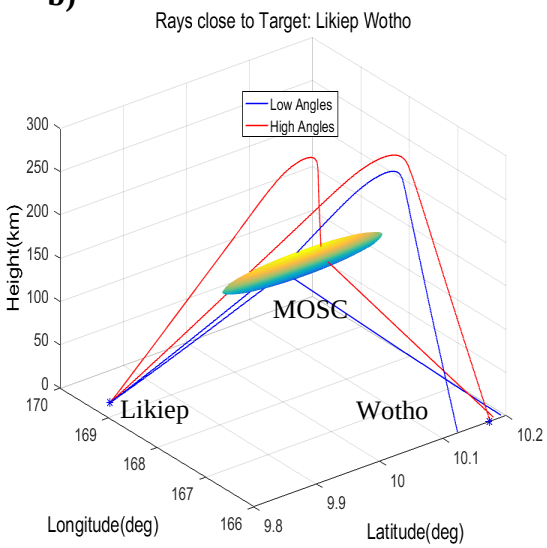
Rays close to Target: Likiep Wotho
Low Angles
High Angles
MOSC
Likiep
Wotho
Height(km)
Longitude(deg)
Latitude(deg)

c)

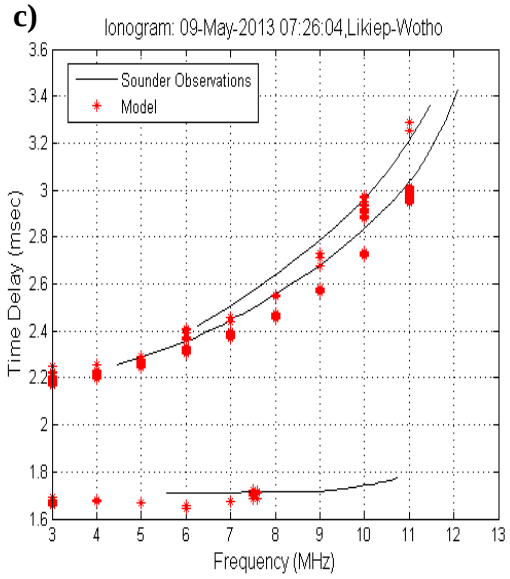
Ionogram: 09-May-2013 07:26:04,Likiep-Wotho
Sounder Observations
Model
Time Delay (msec)
Frequency (MHz)

d)

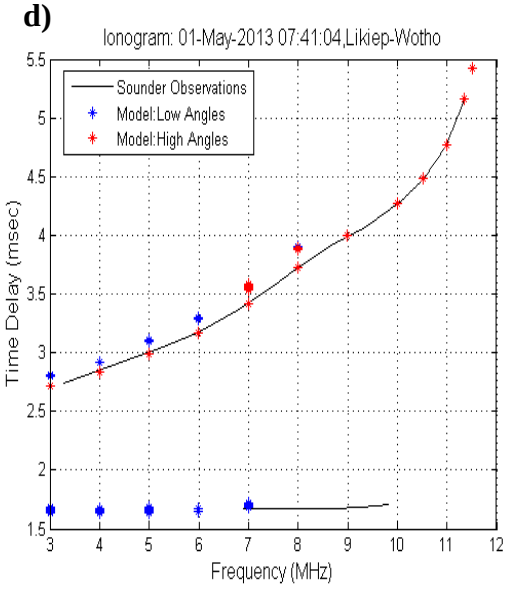
Ionogram: 01-May-2013 07:41:04,Likiep-Wotho
Sounder Observations
Model:Low Angles
Model:High Angles
Time Delay (msec)
Frequency (MHz)

Figure 10.

Relative Received Signal Strength of Likiep/Rongelap at Wotho

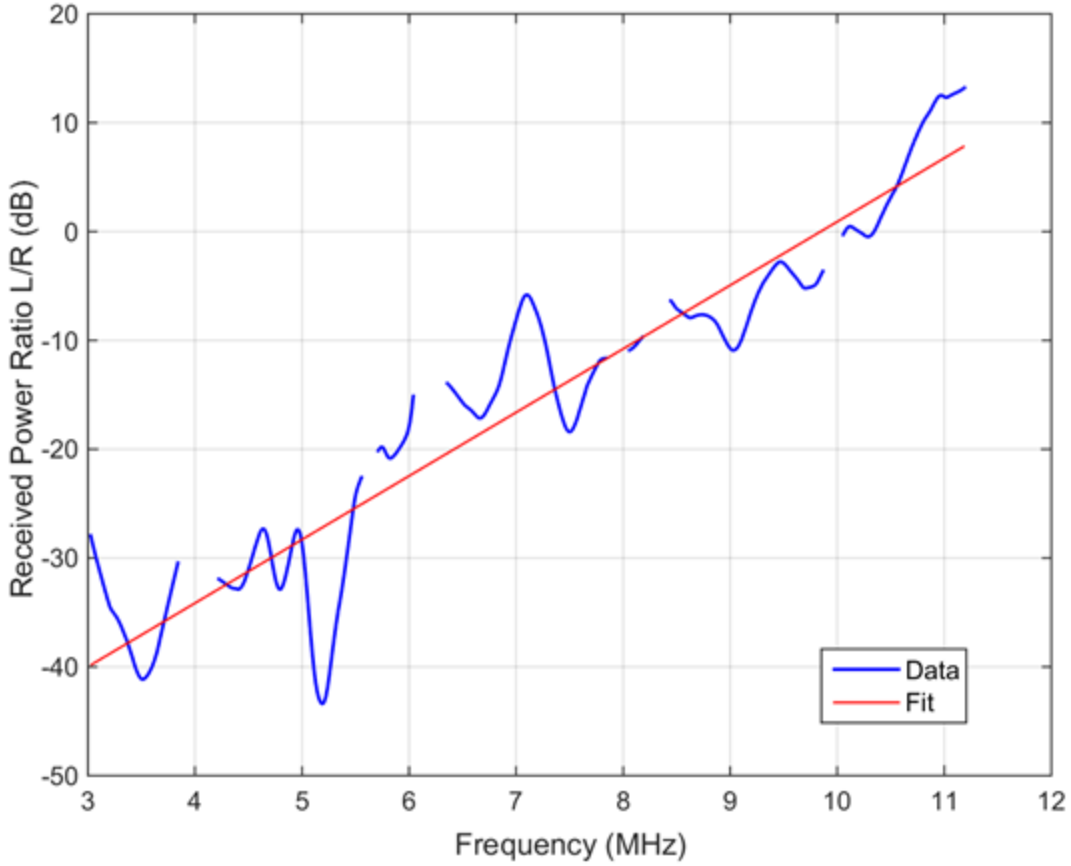

Figure 11.

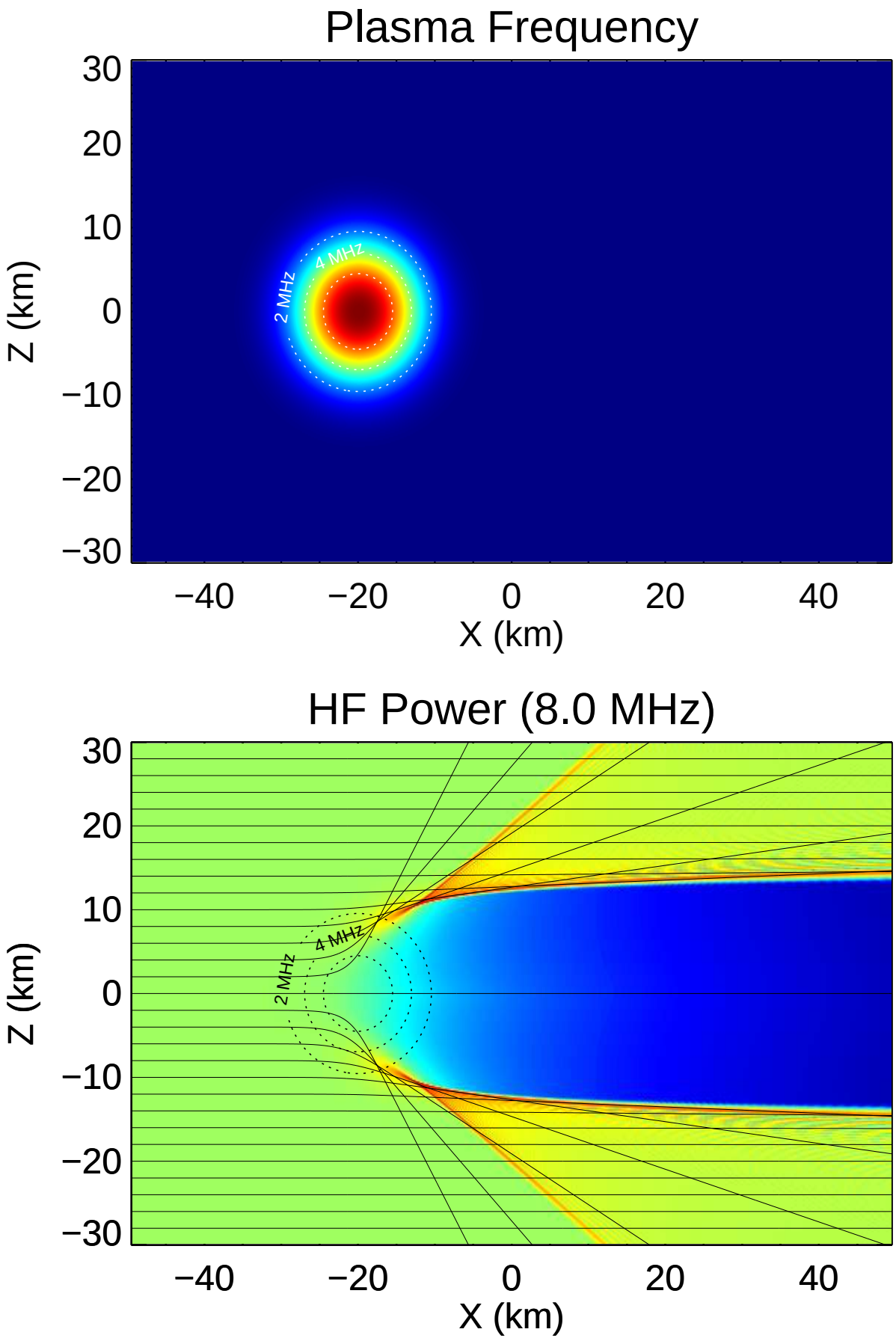
Plasma Frequency
30
20
10
0
−10
−20
−30
Z (km)
2 MHz
4 MHz
−40
−20
0
20
40
X (km)
HF Power (8.0 MHz)
30
20
10
0
−10
−20
−30
Z (km)
2 MHz
4 MHz
−40
−20
0
20
40
X (km)